

Weak localization in transition metal dichalcogenide monolayers and their heterostructures with graphene

Stefan Ilić, Julia S. Meyer, and Manuel Houzet
Univ. Grenoble Alpes, CEA, INAC-Phelips, F-38000 Grenoble, France
(Dated: May 12, 2022)

We calculate the interference correction to the conductivity of doped transition metal dichalcogenide monolayers (TMDC). Because of the interplay between valley structure and intrinsic spin-orbit coupling (SOC), these materials exhibit a rich weak localization (WL) behavior that is qualitatively different from conventional metals or similar two-dimensional materials such as graphene. Our results can also be used to describe graphene/TMDC heterostructures, where the SOC is induced in the graphene sheet. We discuss new parameter regimes that go beyond existing theories, and can be used to interpret recent experiments in order to assess the strength of SOC and disorder. Furthermore, we show that an in-plane Zeeman field can be used to distinguish the contributions of different kinds of SOC to the WL magnetoresistance.

I. INTRODUCTION

Transition metal dichalcogenide monolayers (TMDC) are a class of two-dimensional semiconductors of the form MX_2 , where M is a transition metal and X is a chalcogen. Similarly to graphene, TMDCs have a hexagonal lattice structure, and a number of them (M=Mo, W; X=S, Se, Te) have minima/maxima of the conduction/valence band at the two corners (valleys) $\pm\mathbf{K}$ of the Brillouin zone. Unlike graphene, however, TMDCs have two inequivalent lattice sites and no inversion symmetry, which allows for a large band gap in their spectrum^{1,2}.

Because of the heavy constituent atoms, these materials also host strong intrinsic spin-orbit coupling (SOC), which acts as an effective out-of-plane Zeeman field with opposite orientation in the two valleys³⁻⁵. This valley-dependent SOC enables a variety of applications of TMDCs in optoelectronics and so-called valleytronics, as electrons from different valleys can be excited selectively with circularly polarized light^{6,7}. When sufficiently doped, several TMDCs become superconducting⁸⁻¹¹, where intrinsic SOC plays an important role, as it causes unconventional “Ising pairing” of the Cooper pairs and a great enhancement of the in-plane upper critical field^{8,12}.

The possibility of inducing SOC in a graphene sheet by coupling it to TMDCs in heterostructures has recently sparked scientific interest, as it can lead to phenomena such as edge states^{13,14} and the spin Hall effect^{15,16}. The induced SOC originates from hybridization of the transition metal and carbon orbitals¹⁴. It has two contributions: Kane-Mele SOC¹⁷, which can open a topological gap at the Dirac points $\pm\mathbf{K}$, and so-called valley-Zeeman SOC, which breaks the inversion symmetry of graphene and causes spin-splitting in the band structure.

Transport measurements in highly doped TMDCs¹⁸⁻²⁰ and graphene/TMDC heterostructures^{14,21-25} can give information about the amplitude and mechanism of SOC by studying the quantum correction to the conductance, due to weak localization (WL) and/or antilocalization (WAL) of electrons. W(A)L can be probed by applying a perpendicular magnetic field B_\perp , which suppresses

the quantum correction by breaking time reversal symmetry. By measuring the resulting magnetoconductance as a function of B_\perp and fitting it to theoretical models, one can extract parameters such as scattering and spin relaxation rates.

So far, the experiments have been interpreted using the so-called Hikami-Larkin-Nagaoka (HLN)²⁶ formula (for TMDC experiments) or a similar formula provided by the McCann-Fal’ko (MF)²⁷ theory in the regime of strong intervalley scattering (for graphene/TMDC experiments). HLN theory holds for two-dimensional single-band systems in the presence of SOC. If SOC is weak, constructive electron interference along time-reversed trajectories gives rise to a decrease in conductance (WL). Strong SOC leads to a phase shift due to the spin precession, which results in destructive interference and an increase in conductance (WAL). In Dirac materials, such as TMDCs and graphene, the physical picture becomes more complex. Here, the quantum correction is sensitive to the sublattice degree of freedom, or so-called lattice isospin. Due to the associated Berry phase, it can introduce phase shifts similarly to the spin physics. Furthermore, the multivalley nature of these materials and intervalley scattering also influence the quantum correction. MF theory takes these effects into account for the case of graphene, and gives a full description of WL and WAL with any disorder that satisfies time-reversal symmetry. In the presence of spin-orbit impurities and in the regime of strong intervalley scattering, such that the valley physics is suppressed, it reduces to the HLN formula.

However, the applicability of MF and HLN theories to TMDC and graphene/TMDC is limited, since they were both developed to describe spin-degenerate systems and do not capture spin-splitting caused by the presence of valley-Zeeman SOC. A theory for TMDCs that takes it into account was given by Ochoa *et al.*²⁸ in the regime close to the bottom/top of the conduction/valence band, $|\mu| \approx E_g$, where μ is the chemical potential and $2E_g$ is the band-gap. This parameter regime, however, does not fully describe graphene/TMDC heterostructures and highly doped TMDCs, where $|\mu| \gg E_g$.

In this work, we present a general theory of the interfer-

ence correction for a massive Dirac material with valley-Zeeman SOC. Furthermore, we account for the effect of an in-plane Zeeman field. Our formula can be applied to TMDC and graphene/TMDC heterostructures. Namely, we generalize Ref. 28 to any chemical potential μ , and we show that several contributions to the interference-induced magnetoresistance are sensitive to the magnitude of doping, and are modified or suppressed as the doping increases. We discuss in detail the regime where intervalley scattering dominates over any spin-dependent scattering, which is the most commonly invoked regime when interpreting the experimental data. We find that the interplay between valley-Zeeman SOC Δ_{VZ} and intervalley scattering, parametrized by the scattering time τ_{iv} , leads to new regimes of WL and WAL. In the limit $\tau_{iv}^{-1} \gg \Delta_{VZ}$, MF still holds and HLN is valid if $\tau_{iv}^{-1} \gg \tau_\phi^{-1}$, where τ_ϕ accounts for inelastic dephasing of electrons. However, we find new behavior not captured by these formulas if $\Delta_{VZ} \gtrsim \tau_{iv}^{-1}$. Since both TMDCs and graphene/TMDC are expected to have substantial valley-Zeeman SOC^{4,13,14}, our newfound regimes are experimentally relevant and can be used to extract parameters from the interference-induced magnetoresistance in both systems.

This article is organized in the following way: In Sec. II, we introduce the model Hamiltonian for disordered TMDC and graphene/TMDC heterostructures. In Sec. III, we calculate the interference correction for these materials using the standard diagrammatic technique for disordered systems. We discuss our results in Sec. IV.

II. THE MODEL

The low-energy Hamiltonian describing TMDC monolayers and graphene/TMDC heterostructures in the vicinity of the $\pm\mathbf{K}$ points, and in the presence of a parallel magnetic field is given by^{4,13} $H_{\mathbf{q}} = H_0 + H_{SOC} + H_W + H_{||}$, where

$$\begin{aligned} H_0 &= v(q_x \sigma_x \eta_z + q_y \sigma_y) + E_g \sigma_z, \\ H_{SOC} &= \Delta_{KM} \sigma_z s_z \eta_z + \Delta_{VZ} s_z \eta_z + \lambda(\sigma_x s_y \eta_z - \sigma_y s_x) \\ &\quad + \zeta(q_x \sigma_x s_z + q_y \sigma_y s_z \eta_z), \\ H_W &= \kappa(q_x^2 - q_y^2) \sigma_x - 2\kappa q_x q_y \sigma_y \eta_z, \\ H_{||} &= h s_x. \end{aligned} \quad (1)$$

Here, we use units where $\hbar = k_B = 1$. The two Dirac cones are described by H_0 , where $\mathbf{q} = (q_x, q_y) = q(\cos\theta, \sin\theta)$ is a small momentum displacement measured from $\pm\mathbf{K}$, v is the velocity associated with the linearized kinetic dispersion, and E_g is the difference in on-site energy responsible for opening the band gap. Spin-orbit coupling is described by H_{SOC} , where Δ_{KM} and Δ_{VZ} characterize Kane-Mele and valley-Zeeman SOC, respectively. Rashba SOC, which is related to a mirror symmetry breaking due to the substrate or external fields, is described by λ . The spin-dependence of the velocity is accounted for by ζ . H_W describes the so-called

trigonal warping. Finally, $H_{||}$ is the in-plane Zeeman field, where the Zeeman energy $h = \frac{1}{2}g\mu_B B_{||}$ is determined by the amplitude of the in-plane magnetic field and the g -factor, which is expected to take the value $g \approx 2$ in these materials. We introduce Pauli matrices $\sigma_{x,y,z}$, $s_{x,y,z}$ and $\eta_{x,y,z}$ acting in sublattice, spin, and valley space, respectively. The Hamiltonian (1) contains all terms up to the first order in \mathbf{q} allowed by the symmetries of the system, as well as H_W and $H_{||}$, which break rotational and time-reversal symmetry, respectively.

We assume that the Dirac Hamiltonian H_0 gives the dominant contribution to the energy of the system. This includes the assumption $E_g \gg \Delta_{KM}$, which is the case in both TMDC and graphene/TMDC heterostructures according to first-principle calculations^{4,13}. H_0 is diagonalized by a unitary transformation $U_{\mathbf{q}} = e^{-i\eta_z \alpha_{\mathbf{q}}} e^{i\beta_{\mathbf{q}} \sigma_y \eta_z} e^{i\alpha_{\mathbf{q}} \sigma_z \eta_z}$, where $\tan(2\alpha_{\mathbf{q}}) = q_y/q_x$ and $\tan(2\beta_{\mathbf{q}}) = vq/E_g$. It has a simple spectrum, $\pm E_{\mathbf{q}} = \pm\sqrt{q^2 v^2 + E_g^2}$. After projecting $U_{\mathbf{q}} H_{\mathbf{q}} U_{\mathbf{q}}^\dagger$ onto the conduction band, we obtain the effective Hamiltonian

$$\begin{aligned} \mathcal{H}_{\mathbf{q}} &= \xi_{\mathbf{q}} + \Delta_{so} s_z \eta_z + \lambda \frac{vq_F}{\mu} (s_y \cos\theta - s_x \sin\theta) \\ &\quad + \kappa \frac{vq_F^3}{\mu} \cos 3\theta \eta_z + h s_x. \end{aligned} \quad (2)$$

Here, the energy is measured from the chemical potential, $\xi_{\mathbf{q}} = E_{\mathbf{q}} - \mu$. Furthermore, we have introduced the Fermi momentum $q_F = \sqrt{\mu^2 - E_g^2}/v$ and $\Delta_{so} = \Delta_{KM} E_g/\mu + \Delta_{VZ} + \zeta vq_F^2/\mu$. The chemical potential μ is assumed to be sufficiently above the band gap E_g , so that it is the dominant energy scale, $|\mu - E_g| \gg \Delta_{so}, \lambda, h, \kappa q_F^2$. A Hamiltonian of a similar form can be found in the valence band after the substitution $\xi_{\mathbf{q}} \rightarrow -\xi_{\mathbf{q}}, \mu \rightarrow -\mu$. Although, in the remainder of the text, we will focus only on the conduction band for simplicity, our results also hold in the valence band as long as both spin-split band are occupied. This is readily achieved in graphene/TMDC heterostructures, while a very high doping is required in TMDCs, due to the large spin-splitting caused by the intrinsic SOC in the valence band⁴.

The effect of impurities can be modeled by introducing a random potential disorder, $H_{\mathbf{q}\mathbf{q}'}^{D0} = U_{\mathbf{q}-\mathbf{q}'}^0 + \sum_{i=x,y} V_{\mathbf{q}-\mathbf{q}'}^{0i} \eta_i$, which has intra- and intervalley components, and is diagonal in sublattice and spin space. Upon rotating $U_{\mathbf{q}} H_{\mathbf{q}\mathbf{q}'}^{D0} U_{\mathbf{q}'}^\dagger$ and projecting to the conduction band, a variety of other scattering processes will be generated as combinations of the band structure and potential scattering parameters.

For simplicity, we will take all these processes into account phenomenologically by independent scattering potentials. To do so, we supplement $H_{\mathbf{q}\mathbf{q}'}^{D0}$ with all the other disorder terms allowed by the time-reversal symmetry²⁹, as was done previously in similar studies of weak localization^{27,28}. The disorder Hamiltonian is

then given as $H_{\mathbf{q}\mathbf{q}'}^D = H_{\mathbf{q}\mathbf{q}'}^{D0} + \delta H_{\mathbf{q}\mathbf{q}'}^D$, where

$$\begin{aligned} \delta H_{\mathbf{q}\mathbf{q}'}^D = & \sum_{i=x,y,z} U_{\mathbf{q}-\mathbf{q}'}^i \Sigma_i + \sum_{i=0,x,y,z} \sum_{j=x,y,z} A_{\mathbf{q}-\mathbf{q}'}^{ij} \Sigma_i s_j \eta_z \\ & + \sum_{j=x,y} \left[\sum_{i=0,x,z} V_{\mathbf{q}-\mathbf{q}'}^{ij} \sigma_i \eta_j + \sum_{i=x,y,z} M_{\mathbf{q}-\mathbf{q}'}^{ij} \sigma_y s_i \eta_j \right]. \end{aligned} \quad (3)$$

Here $\Sigma_{0,z,x} = \sigma_{0,x,z}$ and $\Sigma_y = \sigma_y \eta_z$. We characterize the random disorder potentials by Gaussian correlators and assume that different kinds of disorder are uncorrelated:

$$\begin{aligned} \langle U_{\mathbf{q}}^i U_{\mathbf{q}'}^j \rangle &= U_i^2 \delta_{ij} \delta_{\mathbf{q}\mathbf{q}'}, \\ \langle X_{\mathbf{q}}^{ij} X_{\mathbf{q}'}^{kl} \rangle &= X_{ij}^2 \delta_{ik} \delta_{jl} \delta_{\mathbf{q}\mathbf{q}'}. \end{aligned} \quad (4)$$

Here, the brackets $\langle \dots \rangle$ represent disorder averaging and $X = A, V, M$. Furthermore, we use the abbreviation $\bar{\mathbf{q}} = -\mathbf{q}$. The first line in Eq. (3) describes intravalley disorder. The second line describes intervalley disorder, which is due to short-range impurities, such as atomic defects. In both lines, the first and second terms account for spin-independent and spin-dependent contributions, respectively.

We provide estimates of the phenomenological parameters in Eq. (4) in the right-hand side of Table I. We do so by comparing the disorder terms generated by $H_{\mathbf{q}\mathbf{q}'}^D$ after rotation and projection onto the conduction band with the terms generated by $H_{\mathbf{q}\mathbf{q}'}^{D0}$ only, but taking into account corrections up to order $1/\mu$. In this way, we can relate the phenomenological disorder parameters with the main Hamiltonian (1) and the magnitude of the potential disorder.

We proceed by writing the rotated phenomenological disorder potential, $U_{\mathbf{q}} H_{\mathbf{q}\mathbf{q}'}^D U_{\mathbf{q}'}^\dagger$, in the projected basis

$$\begin{aligned} \mathcal{H}_{\mathbf{q}\mathbf{q}'}^D = & \sum_{i=0,x,y,z} \left[U_{\mathbf{q}-\mathbf{q}'}^i f_{\theta,\theta'}^i + \sum_{j=x,y,z} A_{\mathbf{q}-\mathbf{q}'}^{ij} f_{\theta,\theta'}^i s_j \eta_z \right] \\ & + \sum_{j=x,y} \left[\sum_{i=0,x,z} V_{\mathbf{q}-\mathbf{q}'}^{ij} g_{\theta,\theta'}^i \eta_j + \sum_{i=x,y,z} M_{\mathbf{q}-\mathbf{q}'}^{ij} g_{\theta,\theta'}^i s_i \eta_j \right], \end{aligned} \quad (5)$$

where the functions $f_{\theta,\theta'}^i$ and $g_{\theta,\theta'}^i$ capture the anisotropy of the projected disorder potential, which is due to the momentum dependence of the unitary transformation $U_{\mathbf{q}}$. In particular, $2f_{\theta,\theta'}^0 = 1 + e^{-i\eta_z(\theta-\theta')} + \frac{E_g}{\mu}(1 - e^{-i\eta_z(\theta-\theta')})$ and $2f_{\theta,\theta'}^x = \frac{vq_F}{\mu}(e^{-i\eta_z\theta} + e^{i\eta_z\theta'})\eta_z$. Furthermore, $f_{\theta,\theta'}^y = if_{\theta,\bar{\theta}}^y \eta_z$, $f_{\theta,\theta'}^z = f_{\theta,\theta'}^0$, $g_{\theta,\theta'}^0 = f_{-\theta,\theta'}^0$, $g_{\theta,\theta'}^x = f_{-\bar{\theta},\theta'}^x$, $g_{\theta,\theta'}^y = i\eta_z f_{-\theta,\theta'}^x$ and $g_{\theta,\theta'}^z = f_{-\bar{\theta},\theta'}^0$. Here, we used the notation $\bar{\theta} = \theta + \pi$. In simple metals, anisotropic disorder usually only leads to the renormalization of the diffusion constant and the transport time. It has more profound physical consequences in our system, as it captures the sublattice isospin physics and the effect of the Berry curvature.

In order to describe quantum transport in our system, we will employ standard diagrammatic technique for dis-

ordered systems. In particular, we introduce disorder-averaged, zero-temperature retarded (R) and advanced (A) Green's functions as

$$G_{\mathbf{q}\omega}^{R,A} = \left(\omega - \mathcal{H}_{\mathbf{q}} \pm \frac{i}{2\tau} \right)^{-1}. \quad (6)$$

Here, the self-energy $\pm i/(2\tau)$ is calculated from the self-consistent Born approximation, ω is the frequency, and the inverse scattering time τ^{-1} is given by

$$\tau^{-1} = \tau_0^{-1} + \tau_z^{-1} + \tau_{iv}^{-1} + \sum_{i=z,zv,iv} \sum_{j=e,o} \tau_{i,j}^{-1}. \quad (7)$$

The individual contributions to Eq. (7) are defined in the left column of Table I, where we introduced the Fermi velocity $v_F = v^2 q_F / \mu$ and the density of states per valley and per spin at the Fermi level $\nu = \mu / (2\pi v_F^2)$. Furthermore, we will assume that the diagonal disorder rate τ_0^{-1} is the dominant one, i.e., $\tau^{-1} \approx \tau_0^{-1}$, and we will use the diffusive approximation $|\mu - E_g| \gg \tau_0^{-1} \gg \Delta_{so}, h, \lambda, \kappa q^2$.

The current operator in the projected basis is given by $\mathcal{J}_{x\mathbf{q}} = v_F \cos \theta$. Due to the anisotropy of the disorder potential, the current vertex is renormalized, as illustrated in diagrammatic form in Fig. 1(a). Here, the bare vertex is dressed by a series of ladder diagrams, known as diffusons. The renormalized vertex is then given as

$$\tilde{\mathcal{J}}_{x\mathbf{q}} = \frac{\tau_{tr}}{\tau_0} \mathcal{J}_{x\mathbf{q}} \quad \text{with} \quad \tau_{tr} = \left(1 + \frac{v^2 q_F^2}{4E_g^2 + v^2 q_F^2} \right) \tau_0. \quad (8)$$

Here, we have introduced the transport time τ_{tr} , which takes the value τ_0 at the bottom of the conduction band $\mu \approx E_g$, where the spectrum is parabolic (similarly to conventional metals), and $2\tau_0$ deep in the conduction band $\mu \gg E_g$, where the spectrum is linear (as in graphene)³¹. The Drude conductivity is then given as

$$\sigma = \frac{e^2}{2\pi} \int \frac{d^2 \mathbf{p}}{(2\pi)^2} \text{Tr} \left[\tilde{\mathcal{J}}_{x\mathbf{q}} G_{\mathbf{q}\omega}^R \mathcal{J}_{x\mathbf{q}} G_{\mathbf{q}\omega}^A \right] \Big|_{\omega=0} = 4e^2 \nu D, \quad (9)$$

where $D = \frac{1}{2} v_F^2 \tau_{tr}$ is the diffusion constant, and the factor 4 originates from spin and valley degeneracy. The corresponding diagram is shown in Fig. 1(b).

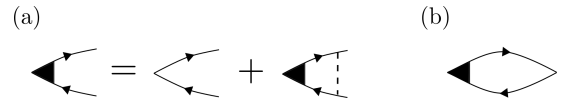


FIG. 1. (a) Vertex renormalization. (b) Drude conductivity diagram. Solid arrows represent Green's functions, while the dashed lines represent disorder. The upper (lower) branch of the diagrams corresponds to retarded (advanced) Green's functions.

III. INTERFERENCE CORRECTION

The interference correction to the Drude conductivity (9) can be expressed in terms of Cooperons, $C_{\alpha\beta,\alpha'\beta'}^{ab,a'b'}$,

Scattering rate	Estimates		
$\tau_0^{-1} = \pi\nu U_0^2(1 + \frac{E_g^2}{\mu^2})$	/		
$\tau_{iv}^{-1} = \pi\nu \sum_{i=x,y} [(V_{0i}^2 + V_{zi}^2)(1 + \frac{E_g^2}{\mu^2}) + (V_{xi}^2) \frac{v^2 q_F^2}{\mu^2}]$	/		
$\tau_{z1}^{-1} = \pi\nu(U_x^2 + U_y^2) \frac{v^2 q_F^2}{\mu^2}$	$\tau_{z2}^{-1} = \pi\nu U_z^2(1 + \frac{E_g^2}{\mu^2})$	$\tau_z^{-1} = \tau_{z1}^{-1} + \tau_{z2}^{-1}$	$U_i^2 \propto U_0^2 (\frac{\kappa q_F^2}{\mu})^2; i = x, y, z$
$\tau_{z,e1}^{-1} = \pi\nu(A_{xz}^2 + A_{yz}^2) \frac{v^2 q_F^2}{\mu^2}$	$\tau_{z,e2}^{-1} = \pi\nu A_{zz}^2(1 + \frac{E_g^2}{\mu^2})$	$\tau_{z,e}^{-1} = \tau_{z,e1}^{-1} + \tau_{z,e2}^{-1}$	$A_{iz}^2 \propto U_0^2 (\frac{\Delta_{KM} v q_F}{\mu^2})^2; i = x, y, z$
$\tau_{z,o1}^{-1} = \pi\nu \sum_{i,j=x,y} (A_{ij}^2) \frac{v^2 q_F^2}{\mu^2}$	$\tau_{z,o2}^{-1} = \pi\nu(A_{zx}^2 + A_{zy}^2)(1 + \frac{E_g^2}{\mu^2})$	$\tau_{z,o}^{-1} = \tau_{z,o1}^{-1} + \tau_{z,o2}^{-1}$	$A_{ij}^2 \propto U_0^2 \frac{\lambda^2}{\mu^2}; i = x, y, z; j = x, y$
$\tau_{zv,e}^{-1} = \pi\nu A_{0z}^2(1 + \frac{E_g^2}{\mu^2})$			$A_{0z}^2 \propto U_0^2 (\frac{\kappa v \Delta_{KM} q_F^3}{\mu^3})^2$
$\tau_{zv,o}^{-1} = \pi\nu(A_{0x}^2 + A_{0y}^2)(1 + \frac{E_g^2}{\mu^2})$			$A_{0i}^2 \propto U_0^2 (\frac{\lambda E_g}{\mu^2})^2; i = x, y$
$\tau_{iv,e}^{-1} = \pi\nu(M_{zx}^2 + M_{zy}^2) \frac{v^2 q_F^2}{\mu^2}$			$M_{zi}^2 \propto V_{0i}^2 (\frac{\kappa v \Delta_{KM} q_F^3}{\mu^3})^2; i = x, y$
$\tau_{iv,o}^{-1} = \pi\nu \sum_{i,j=x,y} (M_{ij}^2) \frac{v^2 q_F^2}{\mu^2}$			$M_{ij}^2 \propto V_{0j}^2 \frac{\lambda^2}{\mu^2}; i, j = x, y$

TABLE I. Left: Dominant diagonal scattering rate, τ_0^{-1} , and other 11 independent scattering rates³⁰ originating from the disorder Hamiltonian (3). The notation for the scattering rates was taken and adapted from Ref. 27. The index z indicates that the related disorder potential is sublattice dependent. zv and iv indicate coupling to the valley matrices η_z and $\eta_{x,y}$, respectively. Indices e and o indicate coupling to the spin matrices s_z and $s_{x,y}$, respectively. Spin-independent disorder is represented by the rates τ_0^{-1} , τ_z^{-1} and τ_{iv}^{-1} , which describe diagonal, intervalley, and sublattice-dependent intravalley disorder. Spin-dependent disorder is represented by the rates $\tau_{i,j}^{-1}$ ($i = z, zv, iv; j = e, o$), which describes intra- ($i = z, zv$) or intervalley ($i = iv$), and spin-preserving ($j = e$) or spin-flipping ($j = o$) disorder. Right: Estimates of the parameters of the phenomenological disorder potential, making use of the procedure introduced in Sec. II.

which represent disorder averages of two Green's functions and correspond to maximally crossed diagrams³². The Greek indices in the subscript (Latin indices in the superscript) correspond to the spin (valley) degree of free-

dom and take values ± 1 . The Cooperons are determined from a system of coupled Bethe-Salpeter equations, as shown in diagrammatic form in Fig. 2(a). Namely,

$$C_{\alpha\beta, \alpha'\beta'}^{ab, a'b'}(\theta, \theta'; \mathbf{Q}) = W_{\alpha\beta, \alpha'\beta'}^{ab, a'b'}(\theta, \theta') + \int_0^{2\pi} \frac{d\theta''}{2\pi} W_{\alpha\alpha_1, \beta\beta_1}^{aa_1, bb_1}(\theta, \theta'') \Pi_{\alpha_1\beta_1, \alpha_2\beta_2}^{a_1b_1}(\theta''; \mathbf{Q}) C_{\alpha_2\beta_2, \alpha'\beta'}^{a_1b_1, a'b'}(\theta'', \theta'; \mathbf{Q}). \quad (10)$$

Here, summation over repeated indices is assumed, and we have introduced the disorder correlator W and the polarization operator Π as

$$W_{\alpha\beta, \alpha'\beta'}^{ab, a'b'}(\theta, \theta') = \langle [\mathcal{H}_{\mathbf{q}\mathbf{q}'}^D]_{\alpha\alpha'}^{aa'} [\mathcal{H}_{\mathbf{q}\mathbf{q}'}^D]_{\beta\beta'}^{bb'} \rangle \quad \text{and} \quad \Pi_{\alpha\beta, \alpha'\beta'}^{ab}(\theta; \mathbf{Q}) = \nu \int d\xi_{\mathbf{q}} [G_{\mathbf{q}\xi+\omega}^R]_{\alpha\alpha'}^a [G_{\mathbf{q}+\mathbf{Q}\omega}^A]_{\beta\beta'}^b. \quad (11)$$

Note that the Green's functions are diagonal in valley space, so the polarization operator only depends on two valley indices. The weak localization correction $\delta\sigma$ can now be expressed in terms of Cooperons as

$$\delta\sigma = \frac{e^2}{2\pi} \int \frac{d^2\mathbf{Q}}{(2\pi)^2} \int_0^{2\pi} \frac{d\theta}{2\pi} \frac{d\theta'}{2\pi} 4\pi\nu\tau_0^3 \left[2\pi\delta(\theta - \theta') - 2\pi\nu\tau_0 W_{\alpha\beta, \alpha\beta}^{ab, ab}(\theta, \theta') \right] \tilde{\mathcal{J}}_{x\mathbf{q}} \tilde{\mathcal{J}}_{x\mathbf{q}'} C_{\alpha\beta, \beta\alpha}^{ab, ba}(\theta, \bar{\theta}'; \mathbf{Q}). \quad (12)$$

Here, the first contribution in the square bracket comes from the bare Hikami box³² [shown in Fig. 2(b)], while the second one comes from two Hikami boxes dressed by an intravalley impurity line [shown in Fig. 2(c)].

In order to resolve the angular structure of the Cooperons, we proceed by solving Eq. (10) in the presence of the dominant diagonal scattering, τ_0^{-1} , only. The other types of scattering will not affect this structure, but only introduce additional Cooperon gaps. We proceed with this calculation in the same spirit as in Ref. 33. First, we expand the Cooperons and the disorder correlator in

harmonics,

$$C^{ab, a'b'}(\theta, \theta'; \mathbf{Q}) = \sum_{n=-\infty}^{\infty} C_n^{ab, a'b'}(\mathbf{Q}) e^{-in(\theta - \theta')},$$

$$W^{ab, a'b'}(\theta, \theta') = \sum_{n=-\infty}^{\infty} W_n^{ab, a'b'} e^{-in(\theta - \theta')}. \quad (13)$$

Since there is no spin-dependent scattering, the Cooperons do not have spin structure, so we can omit the spin indices. Furthermore, $a = a'$ and $b = b'$ in the absence

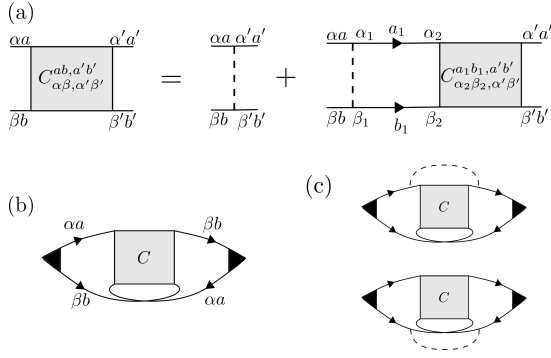


FIG. 2. (a) Bethe-Salpeter equation for the Cooperons. (b) Bare Hikami box. The Hikami boxes with external lines that are diagonal in spin-space give a dominant contribution to the quantum correction in the diffusive limit. (c) Dressed Hikami boxes. For the definition of diagram elements, see Fig. 1. Greek indices in the subscript describe spin, while Latin indices in the supercript describe the valley degree of freedom.

of intervalley scattering. The only Cooperon that enters the interference correction (12) is the intravalley one, $C^{aa,aa}(\theta, \theta')$. From Eqs. (10) and (13), we get a system of coupled equations for its harmonics, whose solution yields

$$C^{aa,aa}(\theta, \theta'; \mathbf{Q}) = C_0^{aa,aa}(\mathbf{Q}) + C_a^{aa,aa}(\mathbf{Q})e^{-ia(\theta-\theta')}$$

with $C_i^{aa,aa}(\mathbf{Q}) = \frac{1}{2\pi\nu\tau_0^2} \frac{1}{D_i|\mathbf{Q}|^2 - i\omega + \tau_\phi^{-1} + \Gamma_i}$. (14)

Here, $a = \pm 1$, $\Gamma_0 = \frac{1}{\tau_0} \frac{(\mu - E_g)^2}{(\mu + E_g)^2}$ and $\Gamma_a = \frac{1}{\tau_0} \frac{2E_g^2}{\mu^2 - E_g^2}$ are the relevant Cooperon gaps, and $D_0 = \frac{1}{8}v_F^2\tau_0(3 + \frac{E_g^2}{\mu^2})$ and $D_a = v_F^2\tau_0 \frac{(E_g^2 + \mu^2)^2}{(\mu^2 - E_g^2)^2}$ are diffusion constants. Furthermore, we introduced the inelastic dephasing rate, τ_ϕ^{-1} .

We see that, in general, both C_0 and C_a will have a large gap of the order τ_0^{-1} and, thus, will be suppressed in the diffusive limit, except in two special cases. Firstly, Γ_0 vanishes at $\mu = E_g$. Close to the band bottom, for $\mu/E_g - 1 \lesssim 2\sqrt{\tau_0}/\tau_\phi$, one finds $\Gamma_0 \lesssim \tau_\phi^{-1}$. Thus, in this regime, the Cooperon C_0 is not suppressed. Secondly, Γ_a vanishes for $\mu \rightarrow \infty$. Thus, deep in the band, at $\mu/E_g \gtrsim \sqrt{2\tau_\phi}/\tau_0$, one finds $\Gamma_a \lesssim \tau_\phi^{-1}$, and the Cooperon C_a is not suppressed. Higher-order harmonics, although non-zero, will always have a non-vanishing gap of the order τ_0^{-1} and will be neglected. We can therefore write

$$C^{aa,aa}(\theta, \bar{\theta}; \mathbf{Q}) = \frac{\Xi}{2\pi\nu\tau_0^2} \frac{1}{D|\mathbf{Q}|^2 - i\omega + \tau_\phi^{-1} + \Gamma_\Xi},$$

where $\Xi = \begin{cases} 1, & \frac{\mu}{E_g} - 1 \lesssim 2\sqrt{\frac{\tau_0}{\tau_\phi}}, \\ 0, & 2\sqrt{\frac{\tau_0}{\tau_\phi}} \ll \frac{\mu}{E_g} - 1 \ll \sqrt{\frac{2\tau_\phi}{\tau_0}}, \\ -1, & \frac{\mu}{E_g} \gtrsim \sqrt{\frac{2\tau_\phi}{\tau_0}}, \end{cases}$ (15)

and $\Gamma_1 = \tau_0^{-1}[vq_F/(2\mu)]^4$, $\Gamma_{-1} = 2\tau_0^{-1}(E_g/\mu)^2$. Note that the diffusion constants D_0 and D_a reduce to D , introduced in Eq. (9), in the relevant limits.

Upon inserting Eq. (15) into Eq. (12), we obtain the quantum correction for massive Dirac fermion systems in the presence of smooth disorder, consistent with Ref. 33. Its behavior is governed by the doping-dependent coefficient Ξ : for a high Dirac mass ($\Xi = 1$) we get WL, whereas in the massless system ($\Xi = -1$), we get WAL. The quantum correction vanishes in the intermediate mass regime. This can be reinterpreted³³ in terms of the Berry phase of a massive Dirac material given as $\varphi_B = \pi(1 - E_g/\mu)$, which introduces no phase shift to the electron interference in the large mass limit (leading to WL), and a shift of π for massless systems (leading to WAL).

Next, we will find the intervalley Cooperon $C^{a\bar{a},a\bar{a}}(\theta, \theta')$. Note that it does not enter the quantum correction (12), but it is useful to resolve its angular structure for later use. We find that the only harmonic that is not gapped is C_0 , and we can write

$$C^{a\bar{a},a\bar{a}}(\theta, \theta'; \mathbf{Q}) = C_0^{a\bar{a},a\bar{a}}(\mathbf{Q}) = \frac{1}{2\pi\nu\tau_0^2} \frac{1}{D|\mathbf{Q}|^2 - i\omega + \tau_\phi^{-1}}. \quad (16)$$

Finally, we proceed to solve the Cooperon equation (10) in the presence of all disorder terms. Additional intervalley Cooperons of the form $C^{a\bar{a},\bar{a}a}$ can now exist. Since they are coupled to $C^{a\bar{a},a\bar{a}}$ via intervalley scattering, which does not introduce additional angular dependence, they will also be angularly-independent. Using Eqs. (15) and (16), we can write for all Cooperons

$$C^{ab,a'b'}(\Xi; \mathbf{Q}) = [C_0^{aa,aa}(\mathbf{Q})\delta_{\Xi,1} + C_a^{aa,aa}(\mathbf{Q})\delta_{\Xi,-1}] \times \delta_{aa'}\delta_{bb'}\delta_{ab} + C_0^{a\bar{a},\bar{a}b}(\mathbf{Q})\delta_{a\bar{b}}\delta_{a'\bar{b}'}$$

$$W^{ab,a'b'}(\Xi) = [W_0^{aa,aa}\delta_{\Xi,1} + W_a^{aa,aa}\delta_{\Xi,-1}] \times \delta_{aa'}\delta_{bb'}\delta_{ab} + W_0^{a\bar{a},\bar{a}b}\delta_{a\bar{b}}\delta_{a'\bar{b}'}. \quad (17)$$

Then, Eq. (10) can be written in a simpler, angularly-independent form,

$$C_{\alpha\beta, \alpha'\beta'}^{ab, a'b'}(\Xi; \mathbf{Q}) = W_{\alpha\beta, \alpha'\beta'}^{ab, a'b'}(\Xi) + W_{\alpha\alpha_1, \beta\beta_1}^{aa_1, bb_1}(\Xi)\Pi_{\alpha_1\beta_1, \alpha_2\beta_2}^{a_1b_1}(\mathbf{Q})C_{\alpha_2\beta_2, \alpha'\beta'}^{a_1b_1, a'b'}(\Xi; \mathbf{Q}). \quad (18)$$

Next, we employ a transformation to the singlet-triplet basis²⁷ in spin and valley space,

$$A_{s's'}^{l'l'} = \frac{1}{4}[s_y s_s]_{\alpha\beta} [\eta_x \eta_l]^{ab} A_{\alpha\beta, \alpha'\beta'}^{ab, a'b'} [s_{s'} s_{y'}]_{\beta'\alpha'} [\eta_l \eta_x]^{b'l'}, \quad (19)$$

where indices $s, s' = 0$ and $l, l' = 0$ correspond to spin- and valley-singlet Cooperon modes, respectively, while $s, s' = x, y, z$ and $l, l' = x, y, z$ correspond to spin- and valley-triplet modes. Here, the operator A can stand for a Cooperon (C), disorder-correlator (W), or a polarization operator (Π). The disorder correlator is diagonal

in the singlet-triplet space, $W_{ss'}^{ll'}(\Xi) = W_s^l(\Xi)\delta_{ss'}\delta_{ll'}$, and the Cooperon equation Eq. (18) after the transformation becomes

$$C_{ss'}^{ll'}(\Xi; \mathbf{Q}) = W_s^l(\Xi)\delta_{ss'}\delta_{ll'} + W_s^l(\Xi)\Pi_{ss_1}^{ll_1}(\mathbf{Q})C_{s_1s'}^{l_1l'}(\Xi; \mathbf{Q}). \quad (20)$$

The quantum correction involves only the diagonal Cooperons $C_{ss}^{ll} \equiv C_s^l$. Note that triplets modes C^x and C^y are related to the intravalley Cooperons, while the valley-singlet C^0 and triplet C^z are related to intervalley ones. We obtain

$$\delta\sigma = -\frac{e^2 D}{\pi} (2\pi\nu\tau_0^2) \int \frac{d^2\mathbf{Q}}{(2\pi)^2} \times \sum_s c_s \left[\sum_{l=0,z} c^l C_s^l(\Xi; \mathbf{Q}) + \Xi \sum_{l=x,y} c^l C_s^l(\Xi; \mathbf{Q}) \right], \quad (21)$$

where $c_s = -1, 1, 1, 1$ and $c^l = 1, 1, 1, -1$ for $s, l = 0, x, y, z$. Eq. (21) generalizes similar expressions from Refs. 27 and 28, which are valid at $\Xi = -1$ and $\Xi = 1$, respectively.

The diagonal Cooperon modes C_s^l , necessary to compute $\delta\sigma$, are determined by solving Eq. (20). Due to the spin-splitting described by Δ_{so} and h , the polarization operator $\Pi_{ss'}^{ll'}(\mathbf{Q})$ is not diagonal in the singlet-triplet space. As a consequence, some Cooperon modes are coupled, as will be discussed in the further text.

First, we solve the Cooperons that are not coupled by the valley-Zeeman SOC or the in-plane field, with the indices $(s, l) = (y, x), (y, y), (z, 0), (z, z)$. They are given by

$$C_s^l = \frac{1}{2\pi\nu\tau_0^2} \frac{1}{\mathcal{P}_s^l}. \quad (22)$$

Here, we have introduced $\mathcal{P}_s^l = D|\mathbf{Q}|^2 - i\omega + \tau_\phi^{-1} + \Gamma_s^l$, where the Cooperon gaps Γ_s^l are specified in Table II. Because the intravalley Cooperons have different angular dependence in the two extreme limits of Eq. (15), their

gaps Γ_s^x and Γ_s^y will also depend on the relevant limit (right-hand side of Table II). Intervalley Cooperons, on the other hand, do not depend on angles and chemical potential and have the same gaps for any μ (left-hand side of Table II).

The Cooperon gaps contain the scattering rates originating from the phenomenological disorder potential (3). Their estimates, listed in Table I, are inversely proportional to the scattering times τ_0 and τ_{iv} . These rates are therefore induced and reinforced by disorder, and behave similarly to the Eliot-Yaffet spin relaxation mechanism^{34,35}. Additionally, scattering rates that are proportional to the potential scattering time τ_0 also enter the gaps:

$$\tau_{BR}^{-1} = 2 \left(\frac{\lambda\nu q_F}{\mu} \right)^2 \tau_{tr}, \quad \tau_{VZ}^{-1} = 2\Delta_{so}^2 \tau_0, \quad (23)$$

and $\tau_W^{-1} = 2 \left(\frac{\kappa\nu q_F^3}{\mu} \right)^2 \tau_0.$

They are related with Rashba SOC, valley-Zeeman SOC, and trigonal warping, respectively. These rates appear since electrons, due to the details of the band structure, acquire an additional phase upon propagation in-between two scattering events. Disorder suppresses this effect, similarly to the Dyakonov-Perel³⁶ spin relaxation mechanism.

Next, we address the coupled Cooperon modes. The effect of the in-plane Zeeman field h applied along the x -direction is such that it couples the spin-singlet C_0 and spin-triplet C_x , as discussed for conventional metals³⁷. Intrinsic SOC behaves similarly to an effective Zeeman field in z -direction, but acts differently from the true Zeeman field as it does not break the time-reversal symmetry, and therefore does not affect the spin- and valley-singlet C_0^0 , which is protected by this symmetry. It couples the Cooperons $C_x^{0(z)}$ with $C_y^{z(0)}$, and $C_0^{x(y)}$ with $C_z^{y(x)}$, as discussed in Ref. 28. The equations for all the coupled Cooperon modes can be compactly written in a matrix form

$$\begin{bmatrix} \mathcal{P}_0^{x(y)} & \mp 2\Delta_{so} & -2ih \\ \pm 2\Delta_{so} & \mathcal{P}_z^{y(x)} & 0 \\ -2ih & 0 & \mathcal{P}_x^{y(y)} \end{bmatrix} \begin{bmatrix} C_{00}^{xx(yy)} & C_{0z}^{xy(yx)} & C_{0x}^{xx(yy)} \\ C_{z0}^{yx(xy)} & C_{zz}^{yy(xx)} & C_{zx}^{yx(xy)} \\ C_{x0}^{xx(yy)} & C_{xz}^{xy(yx)} & C_{xx}^{xx(yy)} \end{bmatrix} = \frac{1}{2\pi\nu\tau_0^2} = \begin{bmatrix} \mathcal{P}_x^{0(z)} & -2\Delta_{so} & -2ih \\ 2\Delta_{so} & \mathcal{P}_y^{z(0)} & 0 \\ -2ih & 0 & \mathcal{P}_0^{0(z)} \end{bmatrix} \begin{bmatrix} C_{xx}^{00(zz)} & C_{xy}^{0z(z0)} & C_{yz}^{00(zz)} \\ C_{yx}^{z0(0z)} & C_{yy}^{zz(00)} & C_{y0}^{x0(0z)} \\ C_{0x}^{00(zz)} & C_{0y}^{0z(z0)} & C_{00}^{00(zz)} \end{bmatrix}. \quad (24)$$

Eq. (24) summarizes 4 matrix equations, each involving 3 coupled modes. Since the Green's functions are diagonal in valley space, the equations for intra- and intervalley Cooperons are decoupled. This can be seen in Eq. (24), where the left-hand (right-hand) side describes matrix equations for intravalley (intervalley) Cooperon

modes.

Finally, after inverting the matrices in Eq. (24), we obtain all Cooperon modes. Combining them with Eq. (21), and introducing the conductance quantum $\sigma_0 = e^2/(2\pi^2\hbar)$, we arrive at the expression for the interference correction

Relaxation gaps for C^0 and C^z	Relaxation gaps for C^x and C^y at $\Xi = -1$.	
$\Gamma_0^0 = 0$	$\Gamma_x^x = \Gamma_y^y = \Gamma_z^z = \Gamma_0^0 = \tau_*^{-1} + 2\tau_{z,e}^{-1} + \tilde{\tau}_{z,o}^{-1} + \tau_{zv,o}^{-1}$	
$\Gamma_x^0 = \Gamma_y^0 = 2\tau_{z,e}^{-1} + \tilde{\tau}_{z,o}^{-1} + 2\tilde{\tau}_{zv,e}^{-1} + \tau_{zv,o}^{-1} + 2\tau_{iv,e}^{-1} + \tau_{iv,o}^{-1}$	$\Gamma_0^x = \Gamma_0^y = \tau_*^{-1} + 2\tilde{\tau}_{zv,e}^{-1} + 2\tau_{zv,o}^{-1}$	
$\Gamma_z^0 = 2\tilde{\tau}_{z,o}^{-1} + 2\tau_{zv,o}^{-1} + 2\tau_{iv,o}^{-1}$	$\Gamma_z^x = \Gamma_z^y = \tau_*^{-1} + 2\tilde{\tau}_{z,o}^{-1} + 2\tilde{\tau}_{zv,e}^{-1}$	
$\Gamma_0^z = 2\tau_{iv}^{-1} + 2\tau_{iv,e}^{-1} + 2\tau_{iv,o}^{-1}$	Relaxation gaps for C^x and C^y at $\Xi = 1$	
$\Gamma_x^z = \Gamma_y^z = 2\tau_{iv}^{-1} + 2\tau_{z,e}^{-1} + \tilde{\tau}_{z,o}^{-1} + 2\tilde{\tau}_{zv,e}^{-1} + \tau_{zv,o}^{-1} + \tau_{iv,o}^{-1}$	$\Gamma_x^x = \Gamma_y^y = \Gamma_z^z = \tau_{**}^{-1} + \tau_{z,o2}^{-1} + \tau_{zv,o}^{-1} + \tau_{BR}^{-1}$	
$\Gamma_z^z = 2\tau_{iv}^{-1} + 2\tilde{\tau}_{z,o}^{-1} + 2\tau_{zv,o}^{-1} + 2\tau_{iv,e}^{-1}$	$\Gamma_0^x = \Gamma_0^y = \tau_{**}^{-1} + 2\tau_{z,e2}^{-1} + 2\tau_{z,o2}^{-1} + 2\tilde{\tau}_{zv,e}^{-1} + 2\tau_{zv,o}^{-1}$	
	$\Gamma_z^x = \Gamma_z^y = \tau_{**}^{-1} + 2\tau_{z,e2}^{-1} + 2\tilde{\tau}_{zv,e}^{-1} + 2\tau_{BR}^{-1}$	
$\tilde{\tau}_{zv,e}^{-1} = \tau_{zv,e}^{-1} + \tau_{VZ}^{-1}$	$\tau_*^{-1} = \tau_{iv}^{-1} + 2\tau_z^{-1} + 2\tau_{iv,e}^{-1} + \tau_{iv,o}^{-1} + \tau_W^{-1} + \frac{2}{\tau_0} \frac{E_d^2}{\mu^2}$	
$\tilde{\tau}_{z,o}^{-1} = \tau_{z,o}^{-1} + \tau_{BR}^{-1}$	$\tau_{**}^{-1} = \tau_{iv}^{-1} + \tau_{z1}^{-1} + \tau_{z,e1}^{-1} + \tau_{z,o1}^{-1} + 2\tau_{iv,e}^{-1} + \tau_{iv,o}^{-1} + \tau_W^{-1} + \frac{1}{16\tau_0} \frac{v^4 q_F^4}{\mu^4}$	

TABLE II. Left: Relaxation gaps Γ_s^l for intervalley Cooperons, where indices s and l denote spin and valley, respectively. There are 8 intervalley Cooperons. The time-reversal symmetry sets the gap Γ_0^0 to zero, while the $x - y$ symmetry imposes equality of all x and y spin-triplet gaps. As a result, there are only 5 independent gaps. Right: Relaxation rates for intravalley Cooperons, which depend on the doping magnitude, captured by the coefficient Ξ . There are 16 intravalley Cooperons: 8 for $\Xi = 1$ and 8 for $\Xi = -1$. $x - y$ symmetry imposes equality of all x and y triplet gaps, in both spin and valley space. As a result, there are only 6 independent gaps. Since at $\Xi = 0$ intravalley Cooperons do not contribute to the quantum correction, the related gaps are not included in the table. For a definition of the different scattering rates, see Table I.

$$\begin{aligned}
\delta\sigma = 2\pi\sigma_0 D \int \frac{d^2\mathbf{Q}}{(2\pi)^2} & \left[-\Xi \sum_{(\alpha,\beta)} \left(\frac{1}{\mathcal{P}_y^\alpha} + \frac{-\mathcal{P}_z^\beta \mathcal{P}_x^\alpha + \mathcal{P}_0^\alpha \mathcal{P}_x^\alpha + 4h^2 + \mathcal{P}_0^\alpha \mathcal{P}_z^\beta + 4\Delta_{so}^2}{\mathcal{P}_0^\alpha \mathcal{P}_z^\beta \mathcal{P}_x^\alpha + 4h^2 \mathcal{P}_z^\beta + 4\Delta_{so}^2 \mathcal{P}_x^\alpha} \right) \right. \\
& \left. + \sum_{(\gamma,\delta)} (-1)^{\delta\gamma z} \left(-\frac{1}{\mathcal{P}_z^\gamma} + \frac{-\mathcal{P}_y^\delta \mathcal{P}_0^\gamma + \mathcal{P}_x^\gamma \mathcal{P}_0^\gamma + 4h^2 + \mathcal{P}_x^\gamma \mathcal{P}_y^\delta + 4\Delta_{so}^2}{\mathcal{P}_x^\gamma \mathcal{P}_y^\delta \mathcal{P}_0^\gamma + 4h^2 \mathcal{P}_y^\delta + 4\Delta_{so}^2 \mathcal{P}_0^\gamma} \right) \right], \quad (25)
\end{aligned}$$

where $(\alpha, \beta) = (x, y), (y, x)$ and $(\gamma, \delta) = (0, z), (z, 0)$. The above equation is the main result of our work and can be readily evaluated analytically in the absence of the in-plane Zeeman field. The divergent integral over momenta in Eq. (25) can be handled by introducing an upper cutoff associated with the inverse mean free path $l^{-1} = \sqrt{D\tau_0}$, which is the smallest length scale in our system. At $h = 0$, we obtain

$$\begin{aligned}
\frac{\delta\sigma}{\sigma_0} = -2\Xi \ln \left(\frac{\tau^{-1}}{\tau_\phi^{-1} + \Gamma_x^x} \right) - \frac{1}{2} \ln \left(\frac{\tau^{-1}}{\tau_\phi^{-1} + \Gamma_z^z} \right) + \frac{1}{2} \ln \left(\frac{\tau^{-1}}{\tau_\phi^{-1}} \right) - \frac{1}{2} \ln \left(\frac{\tau^{-1}}{\tau_\phi^{-1} + \Gamma_0^z} \right) + \frac{1}{2} \ln \left(\frac{\tau^{-1}}{\tau_\phi^{-1} + \Gamma_z^z} \right) \\
+ \gamma_{iv} \sum_{\pm} \pm \ln \left(\frac{\tau^{-1}}{\tau_\phi^{-1} + \Gamma_{iv}^+ \pm \frac{\Gamma_{iv}^-}{\gamma_{iv}}} \right) + \Xi \gamma_s \sum_{\pm} \pm \ln \left(\frac{\tau^{-1}}{\tau_\phi^{-1} + \Gamma_s^+ \pm \frac{\Gamma_s^-}{\gamma_s}} \right). \quad (26)
\end{aligned}$$

Here, we have introduced $\Gamma_{iv}^\pm = 1/2(\Gamma_x^z \pm \Gamma_x^0)$ and $\Gamma_s^\pm = 1/2(\Gamma_0^x \pm \Gamma_z^x)$, as well as

$$\gamma_{iv,s} = \frac{1}{\sqrt{1 - \left(\frac{2\Delta_{so}}{\Gamma_{iv,s}^-} \right)^2}}. \quad (27)$$

The coefficients γ_{iv} and γ_s capture the effect of the spin splitting. They are real if $1 \geq 4\Delta_{so}^2/\Gamma_{iv,s}^2$, and imaginary otherwise. Although the rates $\Gamma_{iv,s}^-$ can be negative and the coefficients $\gamma_{iv,s}$ can be imaginary, their combination entering Eq. (26) is such that the imaginary parts cancel out, so that the conductance is always real (as it should be). The effect of a finite in-plane Zeeman field will be discussed in Sec. IV C.

Quantum interference is very sensitive to a magnetic field B_\perp perpendicular to the monolayer, as it breaks the coherence of time reversed paths of electrons, responsible for WL and WAL. This is used as a probe of W(A)L in experiments, which measure the magnetoconductance as a function of B_\perp . The perpendicular field couples to the momentum of the electrons, unlike the parallel field B_\parallel , which only couples to spin via the Zeeman effect. It leads to a quantization of momenta $|\mathbf{Q}| \rightarrow Q_n = (n + 1/2)/l_B^2$, where $n = 0, 1, 2, \dots$ denotes the Landau levels and $l_B = \sqrt{\hbar/4eB_\perp}$ is the magnetic length. We assume $l_B \gg l$, such that the diffusive limit is not violated, which imposes a constraint on the maximum field $B_\perp \ll \hbar/(4eD\tau_0)$. We evaluate the magnetoconductance $\Delta\sigma = \delta\sigma(B_\perp) - \delta\sigma(0)$ as

$$\begin{aligned} \frac{\Delta\sigma}{\sigma_0} = & 2\Xi F\left(\frac{B_\perp}{B_\phi + B_x^x}\right) + \frac{1}{2}F\left(\frac{B_\perp}{B_\phi + B_z^0}\right) - \frac{1}{2}F\left(\frac{B_\perp}{B_\phi}\right) + \frac{1}{2}F\left(\frac{B_\perp}{B_\phi + B_0^z}\right) - \frac{1}{2}F\left(\frac{B_\perp}{B_\phi + B_z^z}\right) \\ & - \gamma_{iv} \sum_{\pm} \pm F\left(\frac{B_\perp}{B_\phi + B_{iv}^+ \pm \frac{B_{iv}^-}{\gamma_{iv}}}\right) - \Xi\gamma_s \sum_{\pm} \pm F\left(\frac{B_\perp}{B_\phi + B_s^+ \pm \frac{B_s^-}{\gamma_s}}\right). \end{aligned} \quad (28)$$

Here, we have introduced

$$F(z) = \ln(z) + \psi\left(\frac{1}{2} + \frac{1}{z}\right) \approx \begin{cases} \frac{z^2}{24}, & z \ll 1, \\ \ln z, & z \gg 1, \end{cases} \quad (29)$$

where $\psi(z)$ is the digamma function, and $B_i^j = \hbar\Gamma_i^j/(4eD)$ and $B_{so} = \Delta_{so}/(eD)$ are effective magnetic fields associated with the scattering rates and spin-orbit coupling.

Eq. (28) acquires a simple form if the decoherence rate τ_ϕ^{-1} is either the dominant or the smallest scattering rate. For very long τ_ϕ , such that $\tau_\phi^{-1} \ll \Gamma_s^l$, all the gapped Cooperons can be neglected, and only the third term in Eq. (28) remains. Then, we have $\Delta\sigma/\sigma_0 = -1/2F(B_\perp/B_\phi)$, as in conventional metal with strong SO disorder. For short decoherence times, $\tau_\phi^{-1} \gg \Gamma_s^l$, all the Coperon gaps can be neglected. Different contributions to Eq. (28) then cancel pairwise, and we obtain $\Delta\sigma/\sigma_0 = 2\Xi F(B_\perp/B_\phi)$. This exhibits WL, WAL or a vanishing quantum correction for $\Xi = 1, -1, 0$ respectively, similarly to a Dirac material in a smooth disorder potential.

The magnetoconductance formula Eq. (28) captures the rich localization behavior of TMDCs and graphene/TMDC. Due to the large number of parameters it is difficult to apply it directly to experiments. In the next section, we will present and discuss several realistic regimes in which this result significantly simplifies, and compare them to the existing theories.

IV. DISCUSSION

We will proceed by analyzing the magnetoresistance formula (28) in the regimes of strong (Sec. IV A) and weak short-range disorder (Sec. IV B). We will also address the effect of an in-plane Zeeman field (Sec. IV C).

A. Strong short-range disorder

The regime where intervalley scattering dominates over all spin-dependent scattering rates, $\tau_{iv}^{-1} \gg \tau_{i,j}^{-1}$, with $i = z, zv, iv$ and $j = z, o$, is the most commonly used regime when interpreting the measurements of the quantum correction. In this case, the effect of spin-dependent disorder can be captured with only two scattering rates,

$$\begin{aligned} \tau_{sym}^{-1} &= 2(\tau_{z,e}^{-1} + \tau_{zv,e}^{-1} + \tau_{iv,e}^{-1} + \tau_{VZ}^{-1}), \\ \tau_{asy}^{-1} &= \tau_{z,o}^{-1} + \tau_{zv,o}^{-1} + \tau_{iv,o}^{-1} + \tau_{BR}^{-1}. \end{aligned} \quad (30)$$

Here τ_{sym}^{-1} contains all the spin-dependent scattering processes that satisfy mirror ($z \rightarrow -z$) symmetry and thus preserve the electron spin. On the other hand, τ_{asy}^{-1} contains spin-flip processes that break this symmetry. In this regime, $\Gamma_{iv}^- \approx \Gamma_{iv}^+ \approx \tau_{iv}^{-1}$, and $\gamma_{iv} \approx 1/\sqrt{1 - 4\Delta_{so}^2\tau_{iv}^2}$. Furthermore, we will assume that the effect of trigonal warping captured in τ_*^{-1} and τ_{**}^{-1} for intravalley Cooperons (see the bottom of Table II) is small compared to intervalley scattering. In this case we have $\tau_*^{-1} \approx \tau_{**}^{-1} \approx \tau_{iv}^{-1}$, and the magnetoconductance (28) becomes

$$\frac{\Delta\sigma}{\sigma_0} = 2\Xi F\left(\frac{B_\perp}{B_\phi + B_{iv}}\right) + \frac{1}{2}F\left(\frac{B_\perp}{B_\phi + 2B_{asy}}\right) - \frac{1}{2}F\left(\frac{B_\perp}{B_\phi}\right) - \gamma_{iv} \sum_{\pm} \pm F\left(\frac{B_\perp}{B_\phi + B_{iv}(1 \pm \frac{1}{\gamma_{iv}}) + B_s}\right). \quad (31)$$

Here $\tau_s^{-1} = \tau_{sym}^{-1} + \tau_{asy}^{-1}$, and $B_i = \hbar/(4eD\tau_i)$. We see that the magnetoconductance is determined by the combination of valley and spin physics, described by the intervalley scattering rate τ_{iv}^{-1} , and spin scattering rates τ_{sym}^{-1} and τ_{asy}^{-1} . The interplay between intervalley scattering and valley-Zeeman SOC is captured by the coefficient γ_{iv} . We will proceed by analyzing this interplay in two limits: $\tau_{iv}^{-1} \gg \Delta_{so}$ and $\Delta_{so} \gg \tau_{iv}^{-1}$.

Within these two limits, we can readily address

3 regimes of the decoherence rate: (i) $\tau_\phi^{-1} \ll \tau_s^{-1}$, (ii) $\tau_s^{-1} \ll \tau_\phi^{-1} \ll \tau_{iv}^{-1}$, and (iii) $\tau_{iv}^{-1} \ll \tau_\phi^{-1}$, where the quantum correction acquires a simple form. The cases (i) and (iii), where the decoherence rate is the dominant or the smallest one, respectively, were previously discussed in the general context of Eq. (28). The intermediate regime (ii) is not universal. In the limit $\tau_{iv}^{-1} \gg \Delta_{so}$, it yields $\Delta\sigma/\sigma_0 = F(B/B_\phi)$. This is analogous to con-

ventional metal without SO impurities, and represents a sum of three spin-triplets C_i^0 ($i = x, y, z$), which contribute as $3/2F(B_\perp/B_\phi)$, and a spin-singlet C_o^0 , which contributes as $-1/2F(B_\perp/B_\phi)$. For $\Delta_{so} \gg \tau_{iv}^{-1}$, the two triplets C_x^0 and C_y^0 are suppressed by the SOC, and the quantum correction vanishes.

We obtain more interesting and complex behavior in the crossover regimes $\tau_\phi^{-1} \sim \tau_s^{-1}$ [which includes (i) and (ii)] and $\tau_\phi^{-1} \sim \tau_{iv}^{-1}$ [which includes (ii) and (iii)]. Strong intervalley scattering completely suppresses the valley structure in the first regime, so that the magnetoconductance is determined by the spin physics only. On the other hand, the valley physics dominates in the second regime, as the effect of spin-scattering is washed out by electron decoherence.

a. Limit $\tau_{iv}^{-1} \gg \Delta_{so}$: Here, Eq. (31) simplifies, as $\gamma_{iv} \approx 1$. In the crossover regime $\tau_\phi^{-1} \sim \tau_s^{-1}$, the first and the last term of Eq. (31) are suppressed by the large intervalley scattering, and we obtain

$$\frac{\Delta\sigma}{\sigma_0} = \frac{1}{2}F\left(\frac{B_\perp}{B_\phi + 2B_{asy}}\right) - \frac{1}{2}F\left(\frac{B_\perp}{B_\phi}\right) + F\left(\frac{B_\perp}{B_\phi + \tilde{B}_s}\right), \quad (32)$$

which is governed by spin-orbit scattering and is equivalent to the HLN formula. Here, we have introduced $B_{iv}(1 - 1/\gamma_{iv}) + B_s \approx 2B_{so}^2/B_{iv} + B_s = \tilde{B}_s = \hbar/(4eD\tilde{\tau}_s)$. Eq. (32) exhibits WAL-WL crossover as the magnitude of the perpendicular field is increased. The effect of valley-Zeeman SOC is captured by an additional contribution to the symmetric rate $\tau_{sym}^{-1} \rightarrow \tau_{sym}^{-1} + 2\Delta_{so}^2\tau_{iv}$. This effect was already discussed in Refs. 25 and 38 and used to estimate Δ_{so} from the experimental data in graphene/TMDC heterostructures. However, in both references, the estimated SOC is of the same order of magnitude as τ_{iv}^{-1} , which is outside of the region of validity of this formula ($\tau_{iv}^{-1} \gg \Delta_{so}$). Instead, the full formula provided by Eq. (31) should be used in order to get a more reliable estimate of the valley-Zeeman SOC.

Next, we address the crossover regime $\tau_\phi^{-1} \sim \tau_{iv}^{-1}$. The spin scattering rates can be neglected, and the second and third term of Eq. (31) cancel out, which yields

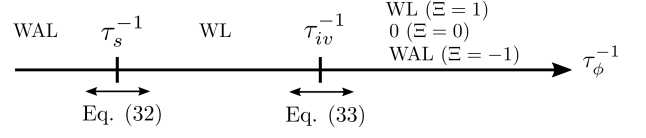
$$\frac{\Delta\sigma}{\sigma_0} = 2\Xi F\left(\frac{B_\perp}{B_\phi + B_{iv}}\right) + F\left(\frac{B_\perp}{B_\phi}\right) - F\left(\frac{B_\perp}{B_\phi + 2B_{iv}}\right). \quad (33)$$

In graphene ($\Xi = -1$) without SOC, it is the same result as in Ref. 31. As a function of a perpendicular field, it exhibits pure WL for $\Xi = 1$ and $\Xi = 0$, and WL-WAL crossover for $\Xi = -1$. Fig. 3(a) gives a schematic representation of the different regimes in the limit $\tau_{iv}^{-1} \gg \Delta_{so}$.

b. Limit $\Delta_{so} \gg \tau_{iv}^{-1}$: Since $\gamma_{iv} \approx 0$, only the first three terms of Eq. (31) contribute to the magnetoconductance. In the crossover regime $\tau_\phi^{-1} \sim \tau_s^{-1}$, we have

$$\frac{\Delta\sigma}{\sigma_0} = \frac{1}{2}F\left(\frac{B_\perp}{B_\phi + 2B_{asy}}\right) - \frac{1}{2}F\left(\frac{B_\perp}{B_\phi}\right), \quad (34)$$

(a) $\tau_{iv}^{-1} \gg \Delta_{so}$:



(b) $\Delta_{so} \gg \tau_{iv}^{-1}$:

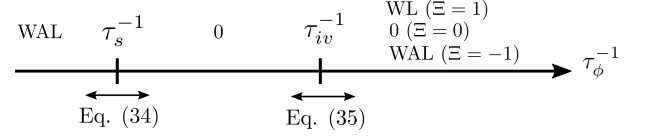


FIG. 3. Schematic representation of the WL behavior in the regime of strong short-range disorder, $\tau_{iv}^{-1} \gg \tau_s^{-1}$. In the crossover regions described by Eqs. (32)-(35), the magnetoconductance at low (high) perpendicular field behaves the same as in the left (right) adjacent region on the τ_ϕ^{-1} arrow.

which corresponds to pure WAL behavior as a function of B_\perp , that saturates on the scale of B_{asy} . This kind of saturation was noticed in several recent quantum correction measurements that exhibit flat WAL curves, such as Refs. 20, 24, and 25.

Finally, we analyze the crossover regime $\tau_\phi^{-1} \sim \tau_{iv}^{-1}$. We find

$$\frac{\Delta\sigma}{\sigma_0} = 2\Xi F\left(\frac{B_\perp}{B_\phi + B_{iv}}\right), \quad (35)$$

which exhibits pure WAL, pure WL, or vanishes for $\Xi = 1$, $\Xi = -1$ and $\Xi = 0$, respectively. Fig. 3(b) gives a schematic representation of the different regimes in the limit $\Delta_{so} \gg \tau_{iv}^{-1}$.

Fig. 4 illustrates the behavior of the magnetoconductance beyond the two extreme limits $\tau_{iv}^{-1} \gg \Delta_{so}$ and $\Delta_{so} \gg \tau_{iv}^{-1}$, analyzed above. Fig. 4(a) addresses the crossover from the regime described by Eq. (32) to Eq. (34) as the magnitude of valley-Zeeman SOC is increased. Similarly Fig. 4(b) shows a crossover from Eq. (33) to Eq. (35).

B. Weak short-range disorder

In this section we analyze the regime where intervalley scattering rate is much weaker than all intravalley spin-scattering rates, $\tau_{i,j}^{-1} \gg \tau_{iv}^{-1}$, where $i = z, zv$ and $j = z, o$. The intervalley spin-scattering rates are assumed to be even weaker, $\tau_{iv,e/o}^{-1} \ll \tau_{iv}^{-1}$, and thus neglected. The

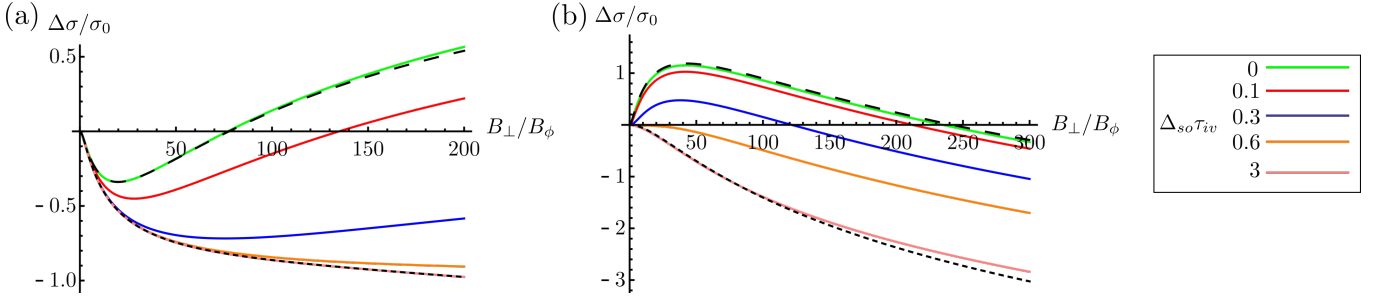


FIG. 4. (a) and (b): Interference-induced magnetoconductance as a function of a weak perpendicular magnetic field under the influence of increasing valley-Zeeman SOC. We take the chemical potential to be deep in the conduction band, such that $\Xi = -1$. (a) All curves are plotted for the parameters $B_{iv} = 200B_\phi$, $B_{sym} = B_{asy} = 3B_\phi$. The dashed black line corresponds to Eq. (32), while the dotted line corresponds to Eq. (34) (b) All curves are plotted for the parameters $B_{iv} = 10B_\phi$, $B_{sym} = B_{asy} = 0.02B_\phi$. The dashed black line corresponds to Eq. (33), while the dotted line corresponds to Eq. (35).

magnetoconductance formula is then given as

$$\frac{\Delta\sigma}{\sigma_0} = 2\Xi F\left(\frac{B_\perp}{B_\phi + B_x^x}\right) - \frac{1}{2}F\left(\frac{B_\perp}{B_\phi}\right) + \frac{1}{2}F\left(\frac{B_\perp}{B_\phi + 2B_{iv}}\right) - \Xi\gamma_s \sum_{\pm} \pm F\left(\frac{B_\perp}{B_\phi + B_s^\pm \pm \frac{B_s^\mp}{\gamma_s}}\right). \quad (36)$$

In this regime, the quantum correction is governed by the interplay between Δ_{so} and a combination of the spin-scattering rates Γ_s^- , described by the coefficient γ_s . Unlike the case of strong short-range disorder, the Cooperons containing γ_{iv} cancel out in this regime, so the ratio of intervalley scattering and valley-Zeeman SOC does not affect $\Delta\sigma$. The three intravalley Cooperon gaps Γ_x^x , Γ_z^x and Γ_0^x that enter Eq. (36) have a similar structure, and depend on the trigonal warping (τ_*^{-1} , τ_{**}^{-1}) and different spin-dependent scattering rates. To simplify the further analysis, we will assume that they are of the same order of magnitude, and introduce the notation $\tau_s'^{-1} = \max(\Gamma_x^x, \Gamma_z^x, \Gamma_0^x)$.

We proceed similarly to the previous section, and analyze the 3 extreme limits with respect to the decoherence rate. If it is the smallest, $\tau_\phi^{-1} \ll \tau_{iv}^{-1}$, or the largest, $\tau_{s'}^{-1} \ll \tau_\phi^{-1}$, scattering rate, the general arguments presented after Eq. (28) apply. In the intermediate limit $\tau_{iv}^{-1} \ll \tau_\phi^{-1} \ll \tau_{s'}^{-1}$, the quantum correction vanishes.

We next examine the crossover regimes. For $\tau_\phi^{-1} \sim \tau_{iv}^{-1}$, we have

$$\frac{\Delta\sigma}{\sigma_0} = -\frac{1}{2}F\left(\frac{B_\perp}{B_\phi}\right) + \frac{1}{2}F\left(\frac{B_\perp}{B_\phi + 2B_{iv}}\right). \quad (37)$$

This formula is determined by intervalley scattering only, and exhibits WAL behavior which saturates on the scale of B_{iv} . Finally, in the crossover regime $\tau_\phi^{-1} \sim \tau_{s'}^{-1}$ we

have

$$\frac{\Delta\sigma}{\sigma_0} = 2\Xi F\left(\frac{B_\perp}{B_\phi + B_x^x}\right) - \Xi\gamma_s \sum_{\pm} \pm F\left(\frac{B_\perp}{B_\phi + B_s^\pm \pm \frac{B_s^\mp}{\gamma_s}}\right). \quad (38)$$

In the limit $\Gamma_s^- \gg \Delta_{so}$, one should consider all three terms in Eq. (38) since $\gamma_s \approx 1$. As Δ_{so} increases, the second line of Eq. (38) becomes suppressed, until it vanishes for $\Delta_{so} \gg \Gamma_s^-$, where $\gamma_s \approx 0$. We see that the qualitative behavior of the magnetoconductance remains the same for any γ_s , and thus, any Δ_{so} . It only depends on the doping coefficient Ξ , and exhibits WL, WAL or neither for $\Xi = 1, -1$ and 0 , respectively. These conclusions are schematically represented in Fig. 5.

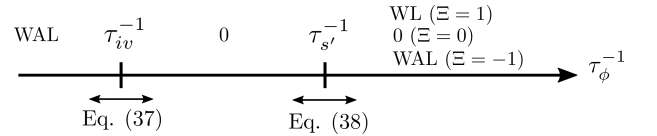


FIG. 5. Schematic representation of the WL behavior in the regime of weak short-range disorder, $\tau_{s'}^{-1} \gg \tau_{iv}^{-1}$. The behavior in the crossover regions is represented in the same way as in Fig. 3.

C. Influence of the in-plane Zeeman field

One of the main difficulties when experimentally extracting the parameters from quantum magnetoresistance fits comes from the fact that there are multiple parameter combinations that can fit the same data. For example, both valley-Zeeman SOC and spin-dependent scattering can lead to pronounced WAL signals. Applying an in-plane Zeeman field can help overcome these ambiguities, as different kinds of disorder and SOC interplay differently with the field.

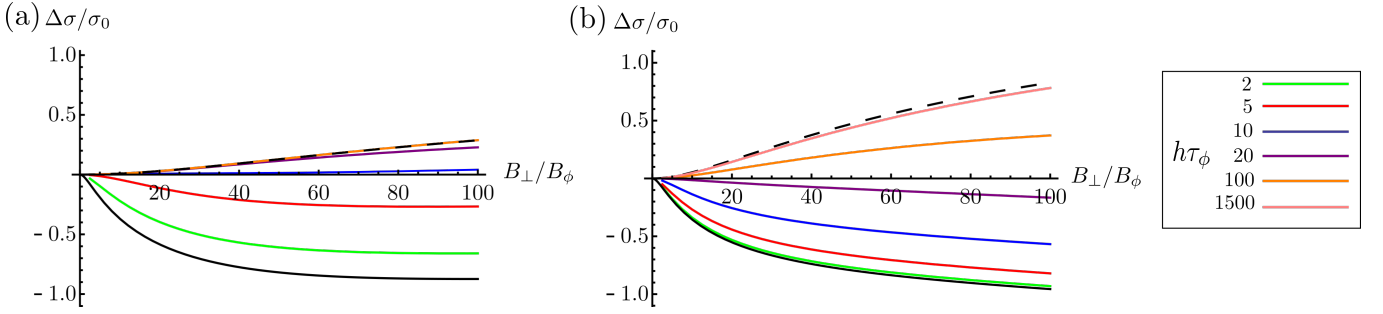


FIG. 6. Influence of the in-plane Zeeman field on the magnetoconductance curves. The solid black line represents the curve at zero in-plane Zeeman field, while the dashed line represents the saturation curve given by Eq. (40) at high fields. (a) The parameters for the plot are $B_{iv} = 100B_\phi$, $B_{sym} = B_{asy} = 10B_\phi$, $B_{so} = 0$ and $\Xi = -1$. The crossover to WL happens at $B_\perp \approx 10B_\phi$. (b) The parameters for the plot are $B_{iv} = 100B_\phi$, $B_{sym} = B_{asy} = 3.5B_\phi$, $B_{so} = 120B_\phi$ and $\Xi = -1$. The crossover to WL happens at $B_\perp \approx 30B_\phi$.

At sufficiently high in-plane Zeeman field, all spin-singlets C_0 and spin-triplets C_x are suppressed, and we arrive at the asymptotic formula for the magnetoconductance

$$\frac{\Delta\sigma}{\sigma_0} = \sum_{i=x,z} \left[\Xi F\left(\frac{B_\perp}{B_\phi + B_i^x}\right) + \frac{1}{2}F\left(\frac{B_\perp}{B_\phi + B_i^0}\right) - \frac{1}{2}F\left(\frac{B_\perp}{B_\phi + B_i^z}\right) \right]. \quad (39)$$

The magnitude of the in-plane Zeeman field required to reach the high-field formula (39) differs depending on the parameter regime, as will be discussed in the following. Note that it will always be reached if $h \gg \Delta_{so}, \tau_i^{-1}$, where τ_i^{-1} are all scattering rates except the diagonal one τ_0^{-1} .

First, we analyze the regime of strong short-range disorder $\tau_{iv}^{-1} \gg \tau_s^{-1}$. In this case the asymptotic formula acquires the form

$$\frac{\Delta\sigma}{\sigma_0} = 2\Xi F\left(\frac{B_\perp}{B_\phi + B_{iv}}\right) + \frac{1}{2}F\left(\frac{B_\perp}{B_\phi + 2B_{asy}}\right) + \frac{1}{2}F\left(\frac{B_\perp}{B_\phi + B_s}\right) - F\left(\frac{B_\perp}{B_\phi + 2B_{iv}}\right). \quad (40)$$

Starting from the general expression (25), we will next check the magnitude of h needed to reach this formula in the limits $\tau_{iv}^{-1} \gg \Delta_{so}$ and $\Delta_{so} \gg \tau_{iv}^{-1}$.

Let us consider $\tau_{iv}^{-1} \gg \Delta_{so}$ and a moderate dephasing rate $\tau_\phi^{-1} \sim \tilde{\tau}_s^{-1}$. In this regime, only the valley-singlets C_s^0 contribute to the magnetoconductance at $h = 0$, as shown in Eq. (32). If the valley-Zeeman SOC does not significantly contribute to the effective rate $\tilde{\tau}_s^{-1}$, that is, if $\tau_s^{-1} \gg \Delta_{so}^2 \tau_{iv}$, it is sufficient to apply the field $h \gg \tau_s^{-1}$ to suppress the spin-singlet C_0^0 and the spin-triplet C_x^0 , and thus reach the high-field formula Eq. (40). On the other hand, if $\Delta_{so}^2 \tau_{iv} \gg \tau_s^{-1}$, the required Zeeman field is much higher, and of the order of intervalley scattering, namely $h \gg \tau_{iv}^{-1}$. If the decoherence rate is larger, $\tau_\phi^{-1} \gg \tilde{\tau}_s^{-1}$, all the spin structure is suppressed by the electron

decoherence, and the in-plane Zeeman field has no effect. In this case, the formula (40) is valid for any h and is equivalent to Eq. (33).

Next, we consider the limit $\Delta_{so} \gg \tau_{iv}^{-1}$. In this regime, the Cooperons C_i^j and C_i^i , where $i = x, y$ and $j = 0, z$, are suppressed by the strong Δ_{so} at $h = 0$. In order to reach the asymptotic formula Eq. (40), a large field $h \gg \Delta_{so}$ is needed. It negates the effect of the valley-Zeeman SOC and restores C_i^j and C_i^i , while suppressing all C_0 and C_x .

Finally, we address the limit of weak short range disorder, $\tau_s^{-1} \gg \tau_{iv}^{-1}$, described by Eq. (36) at $h = 0$. Similarly to the previously considered case, strong h negates the effect of Δ_{so} and suppresses all spin-singlets and x -triplets. Here, the asymptotic formula takes the form

$$\frac{\Delta\sigma}{\sigma_0} = \Xi \sum_{i=x,z} F\left(\frac{B_\perp}{B_\phi + B_i^x}\right), \quad (41)$$

and is reached if the in-plane Zeeman field is the largest energy scale, $h \gg \tau_s^{-1}, \Delta_{so}, \tau_\phi^{-1}$. The prefactor Ξ indicates that it can exhibit WAL, WL or neither depending on the doping, similarly to Eq. (38).

To illustrate a situation where applying the in-plane field can help in the interpretation of the quantum correction, we plot two magnetoconductance curves with a similar shape, but with significantly different parameters in Fig. 6 (black line). The first curve [Fig. 6(a)] has strong spin-scattering and no valley-Zeeman SOC, while the second one has weaker spin-scattering and strong SOC [Fig. 6(b)]. The high-field saturation curve (dashed line) has a similar shape in both cases, and is described by Eq. (40). The amplitude of WL at high fields is larger in the case of strong SOC, as the spin-orbit scattering is weaker, which means that the second line of Eq. (40) gives a larger contribution compared to the other case. More importantly, this case is more resistant to the effect of the applied field, and the crossover to WL happens at a much higher field amplitude. This is consistent with the above analysis, as the expected crossover field is $h \sim \tau_s^{-1}$ for Fig. 6(a) and $h \sim \Delta_{so}$ for Fig. 6(b). Thus, apply-

ing an in-plane field helps distinguish the contributions of valley-Zeeman SOC and spin-dependent scattering to the quantum correction.

V. CONCLUSIONS

In conclusion, we have developed a theory of weak localization and magnetoconductance for TMDC monolayers and their heterostructures with graphene, using standard diagrammatic technique for disordered systems. The interplay between spin and valley physics in these materials yields a rich behavior of the quantum correction to the conductivity, which we discuss in several regimes of interest for the interpretation of recent experimental data. We generalize the HLN and MF theories and

propose a formula, that can be used to extract the magnitude of valley-Zeeman and disorder from the experiments in all regimes. In some cases, interpreting the experiments is not straightforward, as different parameter combinations can explain the data equally well. An in-plane Zeeman field can be used as an additional tuning parameter to help distinguish between the contributions of different processes.

ACKNOWLEDGMENTS

We thank T. Wakamura, H. Bouchiat and S. Gueron for helpful discussions. We acknowledge funding from the Laboratoire d'excellence LANEF in Grenoble (ANR-10-LABX-51-01) and by the ANR through grants No. ANR-16-CE30-0019 and ANR-17-PIRE-0001.

-
- ¹ K. F. Mak, C. Lee, J. Hone, J. Shan, and T. F. Heinz, *Phys. Rev. Lett.* **105**, 136805 (2010).
- ² Q. H. Wang, K. Kalantar-Zadeh, A. Kis, J. N. Coleman, and M. S. Strano, *Nat. Nanotech.* **7**, 699 (2012).
- ³ Z. Zhu, Y. Cheng, and U. Schwingenschlögl, *Phys. Rev. B* **84**, 153402 (2011).
- ⁴ A. Kormányos, G. Burkard, M. Gmitra, J. Fabian, V. Zólyomi, N. D. Drummond, and V. Falko, *2D Mat.* **2**, 022001 (2015).
- ⁵ D. Xiao, G.-B. Liu, W. Feng, X. Xu, and W. Yao, *Phys. Rev. Lett.* **108**, 196802 (2012).
- ⁶ K. F. Mak, K. He, J. Shan, and T. F. Heinz, *Nat. Nanotech.* **7**, 494 (2012).
- ⁷ H. Zeng, J. Dai, W. Yao, D. Xiao, and X. Cui, *Nat. Nanotech.* **7**, 490 (2012).
- ⁸ Y. Saito, Y. Nakamura, M. S. Bahramy, Y. Kohama, J. Ye, Y. Kasahara, Y. Nakagawa, M. Onga, M. Tokunaga, T. Nojima, *et al.*, *Nat. Phys.* **12**, 144 (2016).
- ⁹ J. Lu, O. Zheliuk, I. Leermakers, N. F. Yuan, U. Zeitler, K. T. Law, and J. Ye, *Science* **350**, 1353 (2015).
- ¹⁰ X. Xi, Z. Wang, W. Zhao, J.-H. Park, K. T. Law, H. Berger, L. Forró, J. Shan, and K. F. Mak, *Nat. Phys.* **12**, 139 (2016).
- ¹¹ S. C. de la Barrera, M. R. Sinko, D. P. Gopalan, N. Sivadas, K. L. Seyler, K. Watanabe, T. Taniguchi, A. W. Tsen, X. Xu, D. Xiao, *et al.*, *Nat. Commun.* **9**, 1427 (2018).
- ¹² S. Ilić, J. S. Meyer, and M. Houzet, *Phys. Rev. Lett.* **119**, 117001 (2017).
- ¹³ M. Gmitra, D. Kochan, P. Högl, and J. Fabian, *Phys. Rev. B* **93**, 155104 (2016).
- ¹⁴ B. Yang, M.-F. Tu, J. Kim, Y. Wu, H. Wang, J. Alicea, R. Wu, M. Bockrath, and J. Shi, *2D Mat.* **3**, 031012 (2016).
- ¹⁵ A. Avsar, J. Y. Tan, T. Taychatanapat, J. Balakrishnan, G. Koon, Y. Yeo, J. Lahiri, A. Carvalho, A. Rodin, E. O'Farrell, *et al.*, *Nat. Commun.* **5**, 4875 (2014).
- ¹⁶ J. H. Garcia, A. W. Cummings, and S. Roche, *Nano Lett.* **17**, 5078 (2017).
- ¹⁷ C. L. Kane and E. J. Mele, *Phys. Rev. Lett.* **95**, 226801 (2005).
- ¹⁸ H. Schmidt, I. Yudhistira, L. Chu, A. C. Neto, B. Özyilmaz, S. Adam, and G. Eda, *Phys. Rev. Lett.* **116**, 046803 (2016).
- ¹⁹ Y. Zhang, W. Shi, J. Ye, R. Suzuki, and Y. Iwasa, *Phys. Rev. B* **95**, 205302 (2017).
- ²⁰ D. Costanzo, S. Jo, H. Berger, and A. F. Morpurgo, *Nat. Nanotech.* **11**, 339 (2016).
- ²¹ Z. Wang, D.-K. Ki, J. Y. Khoo, D. Mauro, H. Berger, L. S. Levitov, and A. F. Morpurgo, *Phys. Rev. X* **6**, 041020 (2016).
- ²² B. Yang, M. Lohmann, D. Barroso, I. Liao, Z. Lin, Y. Liu, L. Bartels, K. Watanabe, T. Taniguchi, and J. Shi, *Phys. Rev. B* **96**, 041409 (2017).
- ²³ T. Völkl, T. Rockinger, M. Drienovsky, K. Watanabe, T. Taniguchi, D. Weiss, and J. Eroms, *Phys. Rev. B* **96**, 125405 (2017).
- ²⁴ T. Wakamura, F. Reale, P. Palczynski, S. Guéron, C. Mattevi, and H. Bouchiat, *Phys. Rev. Lett.* **120**, 106802 (2018).
- ²⁵ S. Zihlmann, A. W. Cummings, J. H. Garcia, M. Kedves, K. Watanabe, T. Taniguchi, C. Schönenberger, and P. Makk, *Phys. Rev. B* **97**, 075434 (2018).
- ²⁶ S. Hikami, A. I. Larkin, and Y. Nagaoka, *Prog. Theor. Phys.* **63**, 707 (1980).
- ²⁷ E. McCann and V. I. Falko, *Phys. Rev. Lett.* **108**, 166606 (2012).
- ²⁸ H. Ochoa, F. Finocchiaro, F. Guinea, and V. I. Fal'ko, *Phys. Rev. B* **90**, 235429 (2014).
- ²⁹ Note that the time-reversal operator in this basis is $\mathcal{T} = is_y\eta_x\mathcal{K}$, where \mathcal{K} is complex conjugation.
- ³⁰ The fact that there are 11 distinct scattering rates, excluding the dominant τ_0^{-1} , can be understood as follows. As shown in Table II in Sec. III, there are 5 distinct intervalley and 6 distinct intravalley gaps. Therefore, there should be 11 independent scattering rates to accommodate the same number of independent Cooperon channels.
- ³¹ E. McCann, K. Kechedzhi, V. I. Falko, H. Suzuura, T. Ando, and B. Altshuler, *Phys. Rev. Lett.* **97**, 146805 (2006).
- ³² E. Akkermans and G. Montambaux, *Mesoscopic physics of electrons and photons* (Cambridge university press, 2007).

- ³³ H.-Z. Lu, J. Shi, and S.-Q. Shen, Phys. Rev. Lett. **107**, 076801 (2011).
- ³⁴ R. J. Elliott, Phys. Rev. **96**, 266 (1954).
- ³⁵ Y. Yafet, in *Solid state physics*, Vol. 14 (Elsevier, 1963) pp. 1–98.
- ³⁶ M. D'yakonov and V. Perel, Sov. Phys. JETP **33**, 1053 (1971).
- ³⁷ S. Maekawa and H. Fukuyama, J. Phys. Soc. Jpn. **50**, 2516 (1981).
- ³⁸ A. W. Cummings, J. H. García, J. Fabian, and S. Roche, Phys. Rev. Lett. **119**, 206601 (2017).